

# Chapter 5

## Optical Spectroscopy of Individual Single-Walled Carbon Nanotubes



Kaihui Liu, Yuichiro K. Kato, and Shigeo Maruyama

**Abstract** Carbon nanotubes represent one of the most unique one-dimensional material in the field of nanotechnology. Because of their unique one-dimensionality combined with structure-related electronic and optical properties, single-walled carbon nanotubes exhibit rich physics and attractive applications. Through the overview of the typical spectroscopy such as absorption/Rayleigh scattering, photoluminescence spectroscopy and resonance Raman spectroscopy, we summarize recent efforts in probing and modulating excitonic features of individual single-walled carbon nanotubes. Finally, we will also discuss the recent advances in the study of single-walled carbon nanotubes for future application in photonics.

### 5.1 Introduction

The last thirty years have witnessed intensive research on carbon nanotubes since the first paper published by Sumio Iijima [1]. The electrical and optical properties of a nanotube depend sensitively on the precise tube structure, which can vary from semiconducting to metallic with the slightest change of chiral index. This richness and diversity of carbon nanotubes make them appealing for a variety of very different applications. Although applications based on semiconducting properties of the

---

K. Liu

State Key Laboratory for Mesoscopic Physics, Frontiers Science Center for Nano-optoelectronics, School of Physics, Peking University, 209 Chengfu Rd, Haidian District, Beijing, China  
e-mail: [khliu@pku.edu.cn](mailto:khliu@pku.edu.cn)

Y. K. Kato

Nanoscale Quantum Photonics Laboratory, RIKEN Cluster for Pioneering Research and Quantum Optoelectronics Research Team, RIKEN Center for Advanced Photonics, 2-1 Hirosawa, Wako, Saitama, Japan  
e-mail: [yuichiro.kato@riken.jp](mailto:yuichiro.kato@riken.jp)

S. Maruyama (✉)

Department of Mechanical Engineering, School of Engineering, The University of Tokyo, 7-3-1 Hongo, Bunkyo, Tokyo, Japan  
e-mail: [maruyama@photon.t.u-tokyo.ac.jp](mailto:maruyama@photon.t.u-tokyo.ac.jp)

© Springer Nature Switzerland AG 2021

T. Yatsui (ed.), *Progress in Nanophotonics 6*, Nano-Optics and Nanophotonics,  
[https://doi.org/10.1007/978-3-030-71516-8\\_5](https://doi.org/10.1007/978-3-030-71516-8_5)

135

single-walled carbon nanotube (SWCNT) [2] are still on the way, research on their conductive, mechanical and thermal properties have developed to a certain level.

Especially, spectroscopic characterization of individual SWCNTs have rapidly developed since the resonant Raman spectroscopy of SWCNTs was first measured in 1997 [3]. The strong resonant features of Raman spectra were determined [4], and radial breathing mode (RBM) peak was first used for chirality assignment of individual SWCNTs on substrates in 2002 [5]. Based on this, Kataura plot relating the energy of the band gap and the diameter of carbon nanotubes has been established.

Another spectroscopy technique, photoluminescence (PL) spectroscopy, was also introduced for micelle-suspended SWCNTs in 2002 [6]. It quickly become an essential tool for the determination of chirality distribution of semiconducting carbon nanotubes, in particular for the development of the chirality separation techniques by density-gradient ultracentrifuge (DGU) [7], DNA-based dispersion [8], and gel-chromatography [9]. Soon after, the strong PL from individual SWCNT were studied [10]. Recently, combining with silicon based photonic crystals [11] and defect-based color-centers, single-photon emission of individual SWCNTs were also detected.

In addition, SWCNTs can be probed optically by elastic light scattering. This effect forms the basis of a technique, termed Rayleigh scattering spectroscopy, for the study of individual nanotubes [12]. Spectroscopic information on the electronic transitions of both semiconducting and metallic nanotubes obtained by measuring the elastic scattering cross section as a function of photon energy is another breakthrough in the optics research of SWCNTs [13].

Until recently, optical spectroscopy has developed as a metrology technique (characterization of samples) rather than a unique application for photonic devices. Since chirality specific growth of SWCNT is still a challenge, chirality separation techniques of micelle-dispersed nanotubes are developed along with absorption, PL, and Raman spectroscopy. In addition, people have enjoyed the rich and peculiar physics of the 1D nanomaterial such as strong environmental effect and strong Coulomb interactions which influence spectroscopic features of SWCNT since the typical size of excitons is much larger than the diameter of SWCNTs. In this review, to concentrate on the pristine optical features of SWCNTs, we mainly focus on spectroscopy and photonics of *individual* SWCNTs. After a quick summary of absorption, PL, and Raman optical techniques, we will discuss recent advances in double-walled carbon nanotubes, hetero-nanotubes, Luttinger-liquid plasmons and coupling to silicon photonic devices. This review presents an overview of optical spectroscopy of SWCNTs for future application in photonics.

## 5.2 Optical Spectroscopy of Single-Walled Carbon Nanotubes

A SWCNT can be viewed as a hollow cylinder formed by rolling up a graphene sheet, and its geometrical structures can be uniquely defined by its chiral index  $(n, m)$  [14, 15]. In the zone-folding approach, without considering the many-body

coulomb interactions, the electronic structure of carbon nanotubes can be obtained by cutting the Dirac cone of graphene with a series of parallel  $\mathbf{k}$  lines [14, 15] (Fig. 5.1). For those nanotubes with chiral index  $\text{mod}(n - m, 3) = 0$ , one of the parallel  $\mathbf{k}$ -lines passes through the Dirac point in graphene, resulting in metallic properties. Other nanotubes with  $\text{mod}(n - m, 3) = 1$  and  $2$  are semiconducting ones; named mod1 and mod2, respectively. It's worth noting that some people categorize semiconducting SWCNT based on  $\text{mod}(2n + m, 3) = 1$  and  $2$  as 'type-I' ('SI' or 'mod 2') and 'type-II' ('SII' or 'mod 1'), respectively.

In the Brillouin zone of nanotubes, each parallel  $\mathbf{k}$ -line describes one pair of conduction and valence sub-bands. Given that those parabolic sub-bands provide a series of singularities in the electronic density of states, transitions between sub-band pairs lead to strong optical resonances, which are traditionally labeled as  $S_{ii}$  for semiconducting and  $M_{ii}$  for metallic nanotubes, where  $i$  is the sub-band index (Fig. 5.2).

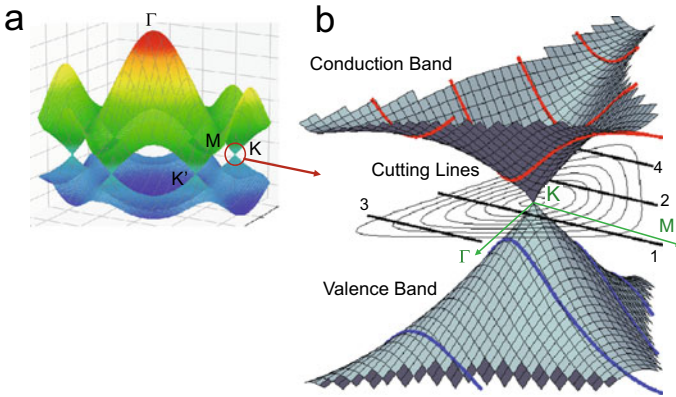


**Fig. 5.1** Electronic structure of single-walled carbon nanotubes. The cutting lines and dispersion are drawn for (7,5) SWCNT. Part of the drawings are courtesy of Prof. Yuhei Miyauchi at Kyoto University and Mr. Kaoru Hisama at UTokyo

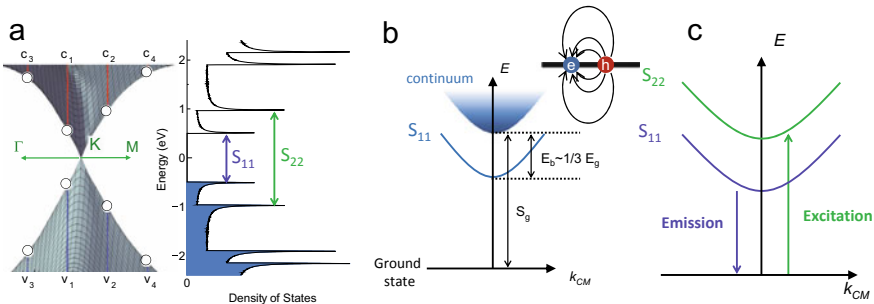


**Fig. 5.2** Density of states and excitonic pictures. **a** Dispersion and density of states for (7,5). **b** Exciton binding energy. **c** Typical PL process

The origin of those distinct optical resonances in carbon nanotubes not only stem from the van Hove singularities, but also from strong excitonic effects. In the one-dimensional (1D) SWCNTs, an electron-hole pair can form a bound state known as exciton. Optical transitions are more accurately described as the generation and recombination of excitons [16]. The traditional labels  $S_{ii}$  and  $M_{ii}$  are still consistent with the excitonic picture since the same sub-bands constitute the excitonic states (Fig. 5.2b).

Excitons in carbon nanotubes are characterized by large binding energies, exceeding 700 meV for a 1 nm diameter pristine tube [17]. The excitonic states are therefore stable at room temperature, in contrast to conventional bulk semiconductors where excitons with binding energy of tens of meV can only be observed at low temperatures [18]. The large binding energies result from weak dielectric screening of the Coulomb interaction; the atomically thin structure of the nanotubes offers weak screening to start with, and the 1D geometry further limits any screening effects [19].

These enhanced light-matter interactions give rise to abundant phenomena that can be probed by optical microscopy and spectroscopy, i.e. direct photon absorption [16, 20, 21], elastic/inelastic scattering of photons (Rayleigh/Raman scattering) [16, 22–24] and luminescence from either optical or electrical excitation [25–31] (fluorescence or electroluminescence). Since optical transitions of SWCNTs are closely related to their geometrical structures, these high-throughput and non-invasive optical techniques have been widely used to characterize their chirality and to probe the physical properties of carbon nanotubes in the past thirty years [13].

Rayleigh scattering, which provides information about the nanotube structure through resonant enhancement of the elastically scattered light when the photon energy matches that of an electronic transition, has emerged as a characterization technique for individual SWCNTs. Rayleigh scattering techniques measure an absolute signal instead of a fractional change and uncover the optical properties of individual nanotubes. Optical absorption, in contrast, is challenging because single tubes change the intensity of the incoming light by  $10^{-5} - 10^{-4}$ . To solve this, high-contrast polarization microscope has been developed for absorption measurement of individual nanotubes suspended or on substrate. The basic principle and related exploration of absorption/Rayleigh scattering of individual SWCNTs will be discussed in Sect. 5.3.

Photoluminescence excitation (PLE) spectroscopy is a widely used optical technique for studying SWCNTs, especially for performing chirality assignments through determination of the absorption and emission energies [6, 15, 32–35]. In addition, PL spectroscopy is a non-intrusive technique that can be performed on as-grown air-suspended individual nanotubes without further sample processing, ideal for characterizing the pristine material. By automating the measurement system, few thousand nanotubes can easily be characterized, allowing for chirality-on-demand measurements. More details of PLE spectroscopy for air-suspended individual SWCNTs will be reviewed in Sect. 5.4.

Resonant Raman scattering spectroscopy of SWCNTs [24] is regarded as the most powerful characterization tool for SWCNT samples. Even from bulk samples, characteristic peaks of phonon features such as G-band D-band, RBM peaks, and

2D-band ( $G'$ ) can be observed. Because RBM frequency directly corresponds to the diameter of SWCNTs, diameter distribution of bulk samples can be roughly estimated by Raman measurements. However, the strong resonant condition depending on excitation laser sometimes hinders the interpretation. The coupling of excitons and phonons has been the central research topic of physics and also metrology. D-band which comes from the double resonance process possible with defects in the hexagonal lattice is a good indication of the quality of SWCNTs. Spectroscopy of individual SWCNTs makes the chirality dependent  $G^+$ ,  $G^-$  features much clearer. Because transition energy and Raman frequency are sensitive to the surrounding environment, discussion of the environmental effect on Kataura plot is crucially important. Details will be discussed in Sect. 5.5.

Although more than a quarter century's intense research and exploration for their distinctive physical properties and potential applications, spectroscopy of carbon nanotubes remain an active research field with many surprises, and opportunities. Recently, the interlayer coupling, modulation of electronic structure and phononic structure of double-walled carbon nanotubes (DWCNTs) has been explored. In addition, hetero-nanotubes based on SWCNTs, like SWCNT surrounded coaxially by hBN nanotube or transition metal dichalcogenides (TMD) nanotubes, give exciting spectroscopy results. Besides, Luttinger-liquid plasmons has been revealed by near field spectroscopy of both metallic and semiconducting SWCNTs. Furthermore, SWCNTs coupled with silicon photonics devices has been developed and single-photon emission at room temperature has been demonstrated. Such recent advances and prospects of spectroscopy of SWCNT will be discussed detailly in Sect. 5.6.

## 5.3 Absorption/Rayleigh Scattering

### 5.3.1 Rayleigh Scattering.

Rayleigh scattering, which relies on elastic scattering of incident light and does not require coupling of incident photons to the phonons in the material, is several orders of magnitude stronger than inelastic Raman scattering [36]. Initially, a tungsten lamp was used as a white light source in Rayleigh spectroscopy for suspended SWCNT bundles, and resonance peaks corresponding to their interband transitions were observed [37]. After that, the use of a laser-based supercontinuum source brought breakthroughs to the field, as it realized parallel collection of spectra over a wide range of wavelengths [16, 22, 23]. At the same time, tight focusing of the incident beam and data collection by oblique objectives provided detection of the elastically scattered light over a large solid angle. With the high spatial and spectral resolution, Rayleigh scattering signal from both metallic and semiconducting freely-suspended nanotubes in the visible region can be detected [22, 23]. Sharp resonant peaks arising from transitions between sub-bands were observed in the Rayleigh scattering spectrum (Fig. 5.3b).

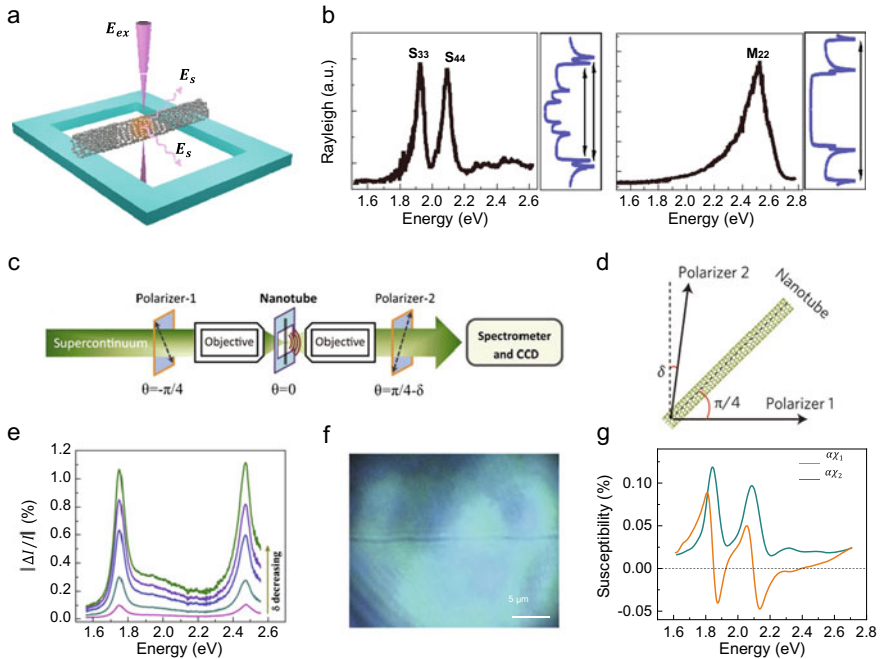


**Fig. 5.3** Rayleigh scattering and optical absorption of SWCNTs. **a**, Scheme of Rayleigh scattering measurement. The supercontinuum incident light ( $E^{\text{ex}}$ ) focuses on suspended individual nanotube and the scattered light ( $E_s$ ) can be collected. **b**, Rayleigh scattering spectrum of an isolated semi-conducting nanotube (left), and a metallic counterpart (right). Scattering is significantly enhanced with the resonance of singularities in the density of states. **c**, Scheme of polarization-optimized homodyne detection for individual nanotube absorption. Two nearly crossed polarizers with a small deviation angle  $\delta$  were used to control the incident and outgoing light polarization, and the suspended individual nanotubes were placed at the focus of the objectives with an angle of  $\pi/4$  with respect to the first polarizer polarization. **d**, Configuration of incident polarizer 1, outgoing polarizer 2 and nanotube for polarization-based optical microscopy. **e**, Homodyne modulation signal ( $\Delta I/I$ ) at various values of deviation angle. With decreasing from 5 to  $0.5^\circ$ , the signal at resonances gradually increases to the 1% level. **f**, Direct optical images of an individual nanotube on silica substrate. **g**, Real ( $\alpha\chi_1$ , orange line) and imaginary ( $\alpha\chi_2$ , green line) susceptibility of the SWCNT (19, 11). Figure adapted with permission from: **b**, ref 22, AAAS; **c**, **e**, ref 20, NAS; **d**, **f**, **g**, ref 64, Springer Nature Ltd.

These ground-breaking experiments sparked intense activity on the research of Rayleigh scattering spectra for SWCNTs [38–42]. For instance, measurements show that the polarization dependence of Rayleigh scattering follows the  $\cos^2 \theta$  form, as expected for dipole emission along the nanotube axis [22]. In addition, direct intertube electronic coupling and dielectric screening bring strong tube-tube interaction, which was directly probed as resonant peak shifts by several tens of meV in the Rayleigh scattering spectroscopy [12]. The backscattering reflection spectrum of suspended individual metallic SWCNTs was collected and an exciton-phonon sideband separated by 0.19 eV from the first optical transition peak was observed, which

provided clear evidence of excitons in metallic SWCNTs. Further, by coating an index-matching medium with the substrate, background scattering was minimized and direct true-color Rayleigh imaging of SWCNTs on quartz was realized [40]. Key SWCNT parameters, including the electronic-types and chiral indices, thus can be mapped quickly. Besides, the spatial distribution of the radiation scattered by the nanotubes was revealed and long-range radiative coupling of SWCNTs was demonstrated. Similarly, by coating an interfacial layer of condensed molecules to enhance the local field, Rayleigh scattering of SWCNTs can be greatly enhanced [42]. Benefitting from that, real-time, true-color Rayleigh imaging and spectroscopy on different substrates ( $\text{SiO}_2/\text{Si}$  and quartz) and environment (water and air) have been successfully achieved, offering rapid feedback of key nanotube properties to specific growth conditions [42].

Complementarily, by combining Rayleigh scattering spectroscopy with electron diffraction, the optical transitions and chiral indices can be directly linked with each other [13, 23]. Up to now, a complete optical-transitions-to-chiral-index atlas has been established [13]. With this structure-property relation map, an experimental Kataura plot was further obtained. This atlas also enables the structure characterization by Rayleigh spectroscopy, which facilitates investigation of the electron-phonon coupling, strain-induced effect, controlled growth [43, 44], and mechanical properties of individual nanotubes [45–47].

### 5.3.2 Absorption Measurement

Optical absorption spectra are critical for various applications of SWCNTs, since optical properties and many optical parameters including absorption coefficient, scattering coefficient, dielectric coefficient, and refractive index, can be derived from them. Given the weak optical absorption of an individual nanotube ( $< 10^{-4}$  for a tightly focused laser beam in the visible region), the signal is buried in the background and laser intensity fluctuations. Thus, compared to Rayleigh scattering that measures the response in a dark-field geometry, it is more difficult to determine the optical absorption of an individual nanotube.

Early absorption experiments were carried out on carbon nanotube films, where energy-dependent and polarization-dependent absorption cross-sections were revealed [48–51]. Thereafter, a UV-vis-NIR absorption spectrum of the micelle-separated single-chirality SWCNTs in solution were obtained and used to determine the purity and chirality [9, 52–54]. For individual SWCNTs, detours had to be made to detect the absorption information in the photocurrent excitation spectrum [55–58] or photothermal signal [59], but these techniques suffer from slow laser-frequency scanning and limited spectral range.

The quantitative measurement of the absorption coefficient for an individual CNT was first realized by using the spatial modulation spectroscopy technique [21, 46, 59–61]. By spatially moving the nano-object in and out of the focal spot of a tightly focused light beam, spatial modulation spectroscopy technique induces a modulation

of the transmission or reflection intensity. By directly measuring these modulation, the absorption spectrum of an individual nanotube can be obtained. Under each given optical frequency, the detected intensity change ( $\Delta I/I$ ) is the result of the interference between the small optical signal ( $E_s$ ) of samples and electric field ( $E_{LO}$ ) of excitation light:

$$\frac{\Delta I}{I} = \frac{|E_{LO} + E_s|^2 - |E_{LO}|^2}{|E_{LO}|^2} = \frac{2|E_s|}{|E_{LO}|} \cos \varphi \quad (5.1)$$

where  $\varphi$  is the relative phase between  $E_s$  and  $E_{LO}$ . The small  $|E_s|^2$  term can be ignored. The resulting mixed modulation signal ( $\Delta I/I$ ), which carries the information (amplitude, phase) of the original desired signal ( $E_s$ ), can be larger than  $E_s$  and then easily detected. Based on this concept, the absorption cross-section of SWCNTs per unit length was successfully determined [20, 21]. Furthermore, by comparing the experimental absorption spectra of the metallic and semiconducting nanotubes, exciton binding energy in metallic SWCNT was deduced to be 50 meV. Besides, by comparing the resonance peaks of the same SWCNT with free-standing samples or those deposited on  $\text{SiO}_2/\text{Si}$  substrate, a large broadening and a red-shift induced by the substrate were revealed.

To enhance the small absorption signal and quantitatively determine the absolute absorption cross-section of individual CNTs in a wide spectral range, the large background signal of excitation light must be suppressed. Utilizing the strong depolarization effect of 1D CNTs, cross-polarization techniques provide the possibility to enlarge the contrast signal by reducing the local excitation electric field ( $E_{in}$ ) while maintaining the signal ( $E_{NT}$ ) of SWCNT [13, 41, 48, 62]. As shown in Fig. 5.3c,d, by setting the SWCNT between two perpendicular polarizers (with a small deviation angle  $\delta$ ) at an angle of  $45^\circ$  with the main axes of the polarizers, the excitation light which keeps the incident polarization can be reduced by several orders of magnitude, thus making the weak nanotube signal observable. With a small  $\delta$ , the greatly enhanced optical contrast  $\Delta I/I$  can reach  $\sim 1\%$  level (compared with  $10^{-4}$  in conventional transmission methods) and become easily detectable (Fig. 5.3e). Combining with the laser spot profile, the absorption cross-section of many individual CNTs could be quantitatively determined. Furtherly, by extrapolating enough data, an empirical formula was established, which can be used to predict the absorption cross-section spectrum for any given nanotubes [41].

Fundamentally, the strength of the absorption is determined by the imaginary part of the susceptibility, and Rayleigh scattering relies on the square of linear optical susceptibility of the nanotube. Recently, based on the cross-polarization strategy, an elliptical polarization-based optical homodyne detection technique was further demonstrated and the detection of both the real and imaginary parts of  $\tilde{\chi}$  of individual carbon nanotubes was realized [63]. By utilizing the interference between incident left-/right-handed polarization beam and nanotube scattering light, two sets of optical spectra containing both  $\chi_1$  and  $\chi_2$  information with different pre-coefficients can be obtained, which allows one to determine the quantitative value of  $\tilde{\chi}$  (Fig. 5.3e). In addition, elliptical polarization light with a relatively large ellipticity and a nearly

crossed polarizer were used, which can greatly reduced the background of excitation light, enhancing the optical signal level by about two orders of magnitude and making the extremely weak individual nanotube signal readily detectable.

### 5.3.3 *In-Situ Optical Imaging*

Direct visualization of individual carbon nanotubes in ambient conditions is of great significance for their manipulation and applications. Compared with the visualization of SWCNTs with the scanning electron microscope (SEM), transmission electron microscope (TEM), atomic force microscope (AFM), scanning tunneling microscope (STM) and so on, optical imaging of carbon nanotubes with high throughput can be quite more convenient to integrate with other facilities, thus making it highly desirable and long been pursued for decades. Because their nanoscale dimensions are much smaller than the wavelength of visible light, it is generally difficult to observe them by optical microscopes.

One approach to address this challenge is to take advantage of the scattering of other nanoparticles. By depositing Ag, Au, TiO<sub>2</sub> nanoparticles [64, 65], or water droplet onto SWCNTs [66], the visualization and manipulation of individual ultralong carbon nanotubes under optical microscopes could be realized. However, such methods are generally subject to complicated deposition processes or short imaging times.

The second pathway is by the light-matter interaction process of SWCNTs and high-end scientific cameras. Based on fluorescence, Raman, electro-luminescence and photocurrent process of SWCNTs [67–69], the morphology of individual nanotubes can be successfully mapped by moving the laser focus. However, they are time-consuming. Notably, by using the Rayleigh signal with relatively strong intensity and the strong optical anisotropy, polarized light microscopy was developed to image individual suspended CNTs. In addition, as mentioned before, true-color imaging of SWCNTs on a substrate, which uses refractive index matching to reduce the reflected light of the substrate has also been reported. Furthermore, polarization-based optical microscope in reflection configuration has been successfully constructed and high-throughput optical imaging and in-situ spectroscopy of individual CNTs in devices have been realized (Fig. 5.3f). By manipulating the polarization, the reflection field was strongly reduced, meanwhile, the nanotube field was kept so that the optical contrast could be sufficiently enhanced. As such, optical contrast spectra of a single CNT can be acquired in situ and its chirality can be determined accurately with the aid of an experimental transition-chirality atlas. So far, this technique has been applied to give feedback to the growth, monitoring device performances, and observation of carbon nanotube etching process [44, 70, 71].

## 5.4 PL Microscopy of Individual-Suspended Carbon Nanotubes

### 5.4.1 Air-Suspended Carbon Nanotubes

Air-suspended SWCNTs grown over trenches on bare Si substrates are used for PL microscopy measurements [72]. The trenches, as well as sample alignment marks, are formed by electron beam lithography and dry etching, where the widths of the trenches range from 0.2 to 6.8  $\mu\text{m}$ . Catalyst areas are patterned by another electron beam lithography step as shown in Fig. 5.4a. As a standard catalyst for nanotube growth, 20 mg of Fe(III) acetylacetonate and 100 mg of fumed silica dispersed in 40 g of ethanol are used. The catalyst particles are deposited using spin-coating and lift-off techniques, and the samples are heated in air at 400  $^{\circ}\text{C}$  for 5 min.

SWCNTs are synthesized by alcohol chemical vapor deposition [73]. Samples are brought into a quartz tube with an inner diameter of 26 mm, and its internal pressure is kept at 110 kPa with a gas mixture of 97% Ar and 3%  $\text{H}_2$  flowing at 300 sccm. The temperature is ramped to 800  $^{\circ}\text{C}$  over 15 min by an electric furnace, and the gas flow and the temperature are kept constant for another 15 min to reduce the catalyst metal. Finally, ethanol vapor is delivered into the quartz tube for 10 min by switching the gas flow to bubble through a bottle of ethanol [74]. Figure 5.4b is a scanning electron micrograph of a sample after the nanotube growth process.

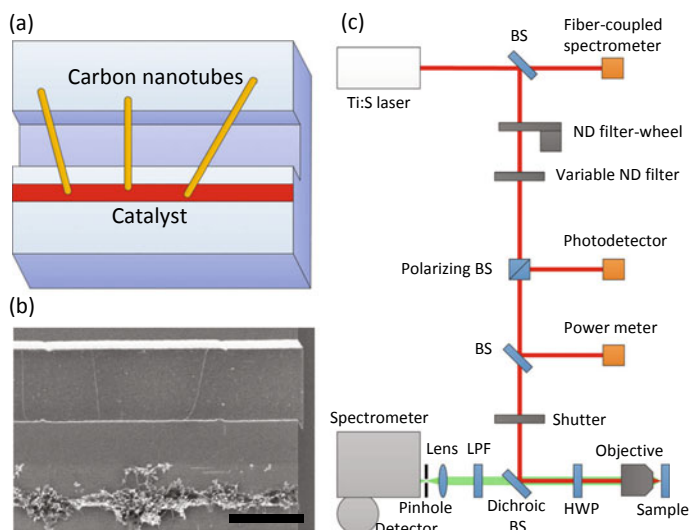


**Fig. 5.4** **a** A schematic of a sample. 10 mm  $\times$  10 mm chips with 144 trenches with a length of 900  $\mu\text{m}$  are used. **b** A scanning electron micrograph of a typical sample. The scale bar is 2  $\mu\text{m}$ . **c** A schematic of the optical setup. The thin line represents the excitation beam and the thick line indicates the PL collection path. Original data presented in [72]

### 5.4.2 *PL Spectroscopy of Individual Nanotubes*

An automated confocal PL measurement system (Fig. 5.4c) has been constructed for characterization of a large number of nanotubes [72]. In the set-up, a continuous-wave Ti:sapphire (Ti:S) laser is used for excitation, whose wavelength is controlled by a motorized linear actuator attached to the birefringent filter of the laser. The output beam passes through a polarizing beam splitter (BS) to clean the polarization and allow the collection of the reflected beams from the sample. The beam is split into two paths, and one of the beams enters a power meter. Calibration has been performed so that the actual excitation power on the samples can be obtained. With a feedback control using the variable neutral-density (ND) filter and the power meter, the excitation power can be tuned within an error of less than 1%. Passing through a shutter used for background subtraction, the transmitted beam is directed towards the sample by a dichroic BS, and then its polarization is rotated by a half-wave plate (HWP) mounted on a motorized rotation stage. An objective lens is used to focus the excitation beam and to collect the emission signals from the nanotubes. The wavelength-dependent  $1/e^2$  diameter of the focused laser has been characterized by performing PL line scans perpendicular to a suspended nanotube.

The samples are mounted on an automated three-dimensional stage with a travel range of  $\pm 10$  mm and a resolution of 50 nm, which is used for focusing as well as sample scanning. PL emitted from the nanotubes transmits the dichroic BS, and a long pass filter (LPF) with a cut-on wavelength at 950 nm is used for further laser rejection. PL from the sample is focused by a lens with a focal length of 50 mm, and it passes through a confocal pinhole with a diameter of 150  $\mu\text{m}$ , corresponding to an aperture with 5.4  $\mu\text{m}$  diameter at the sample image plane. Liquid-nitrogen-cooled InGaAs photodiode array attached to a 300-mm spectrometer with a 150 lines/mm grating blazed at 1.25  $\mu\text{m}$  is used to obtain the PL spectra, which provides a spectral resolution of  $\sim 1$  meV.

The reflected beam from the sample traces back the same path as the excitation beam and is detected by a photodiode. By performing reflectivity scans, position offsets and rotation angles of the samples can be determined from the alignment marks. In addition, by bringing the laser focus at three different positions on the surface, tilt angles are obtained. Coordinate transformation can be performed from the results of these measurements, allowing the entire area of the samples to be scanned while keeping it in focus. All measurements are performed at room temperature in air unless otherwise noted.

### 5.4.3 *Statistical Characterization of Air-Suspended Nanotubes*

The suspended nanotubes are located by line scans along the trenches [Fig. 5.5a], and PLE measurements are performed for each nanotube. The PLE maps of individual

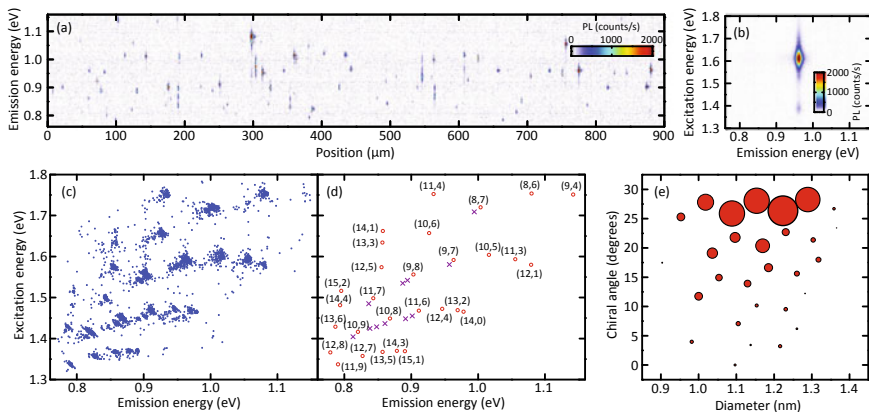


**Fig. 5.5** **a** A typical result of a trench scan with  $P = 50 \mu\text{W}$  and  $E_{ex} = 1.59 \text{ eV}$ . **b** A typical PLE map of a (9,7) nanotube with  $P = 1.5 \mu\text{W}$ . **c** PLE peak positions of 3736 individual nanotubes. **d** Averaged peak positions for each chirality. Open circles represent main spots, and cross marks indicate satellite spots. **e** Chirality distribution as a function of tube diameter and chiral angle. The area of the circles represents the population. Original data presented in [72]

nanotubes present distinct peaks in both emission and excitation energies as shown in Fig. 5.5b, where  $S_{11}$  and  $S_{22}$  energies of the nanotubes are obtained from Lorentzian fits. As PLE maps with multiple peaks and significant broadening may come from bundled tubes [75] or defect states, such nanotubes are excluded from further measurements. These scans are performed automatically overnight, where typically 36 trench scans are done within 9h while 300 PLE maps are taken within 10h. The positions and chiralities for thousands of nanotubes are recorded into a list, allowing for a statistical analysis [72]. Such a list is also utilized for chirality-on-demand measurements later (Sect. 5.6.4).

In Fig. 5.5c, peak positions in the PLE maps are plotted for all of the measured individual nanotubes, where high density spots corresponding to different chiralities can be seen. Chiralities are assigned by utilizing the results on ensembles of nanotubes [32–34], and the averaged peak positions for each chirality are summarized in Fig. 5.5d and Table 5.1. Interestingly, the PLE peak distribution in Fig. 5.5c shows satellite spots with slightly lower energies. The energy shifts between the main spots and the first satellites do not depend much on chirality, and the average values are 8.1 and 12.3 meV for  $S_{11}$  and  $S_{22}$ , respectively. For chiralities with large population such as (9, 8) and (10, 8), there are second and third satellite spots similar to the first satellite spots but with decreasing populations. As no apparent differences in PLE maps between the main spot and the satellites are observed except for the slight redshifts, these satellites are assigned to bundles of nanotubes with the same chirality. This interpretation is consistent with the redshifted values reported in [34], where samples without catalyst patterning are used and more bundles are expected. It is also interesting that the distributions of the peaks for the same chiralities are not isotropic, but show up as elongated ellipses corresponding to anticorrelated  $S_{11}$  and

**Table 5.1** Average  $S_{11}$  and  $S_{22}$  peak energies for individual air-suspended CNTs obtained from Lorentzian fits of their PLE maps. The error values are standard deviations. Original data presented in [72]

$(n, m)$	$S_{11}$		$S_{22}$	
	(nm)	(meV)	(nm)	(meV)
(8,6)	1148.0±4.4	1080.0±4.2	707.0±2.4	1753.6±6.0
(8,7)	1235.1±5.0	1003.8±4.0	720.9±2.0	1719.9±4.7
(9,4)	1085.3±3.5	1142.3±3.7	708.0±5.6	1751.0±13.9
(9,7)	1286.8±3.9	963.5±2.9	779.0±2.6	1591.6±5.3
(9,8)	1372.4±3.8	903.4±2.5	796.8±2.6	1556.1±5.1
(10,5)	1219.8±4.1	1016.4±3.4	773.0±3.3	1604.0±6.9
(10,6)	1337.7±3.7	926.8±2.6	748.2±2.1	1657.1±4.8
(10,8)	1427.8±4.3	868.3±2.6	855.7±2.5	1448.8±4.2
(10,9)	1511.1±5.1	820.4±2.8	875.4±2.2	1416.3±3.5
(11,3)	1174.5±3.5	1055.6±3.1	778.1±3.0	1593.4±6.1
(11,4)	1328.2±4.7	933.4±3.3	707.5±2.3	1752.4±5.7
(11,6)	1360.2±3.9	911.5±2.6	844.7±2.6	1467.8±4.5
(11,7)	1470.1±3.0	843.3±1.7	827.6±2.0	1498.1±3.7
(11,9)	1568.0±5.5	790.7±2.8	927.3±2.8	1337.0±4.1
(12,1)	1148.6±2.9	1079.4±2.7	784.8±2.5	1579.8±5.1
(12,4)	1310.0±3.0	946.4±2.2	842.1±2.1	1472.2±3.7
(12,5)	1448.7±3.6	855.8±2.2	787.7±1.8	1573.9±3.7
(12,7)	1498.7±4.3	827.3±2.4	913.4±1.9	1357.3±2.8
(12,8)	1591.2±3.1	779.2±1.5	907.6±2.2	1366.0±3.4
(13,2)	1278.8±2.4	969.5±1.8	843.9±2.1	1469.1±3.7
(13,3)	1446.6±4.5	857.0±2.6	758.7±3.1	1634.1±6.6
(13,5)	1446.1±3.5	857.4±2.1	906.7±1.6	1367.4±2.4
(13,6)	1576.1±3.8	786.6±1.9	867.7±1.8	1428.8±3.0
(14,0)	1267.3±2.5	978.3±1.9	846.1±1.6	1465.3±2.8
(14,1)	1445.5±3.8	857.7±2.2	745.9±2.2	1662.1±4.9
(14,3)	1411.1±3.4	878.6±2.1	905.0±1.7	1369.9±2.6
(14,4)	1561.9±3.6	793.8±1.8	837.1±1.7	1481.1±3.1
(15,1)	1392.1±2.3	890.6±1.5	905.7±2.1	1369.0±3.1
(15,2)	1558.6±1.8	795.5±0.9	817.7±3.1	1516.2±5.8

$S_{22}$ . This cannot be explained by dielectric screening effects, but seems consistent with the effects of slight strain [76–78] or bending [79].

The automated scans allow us to determine the chirality distribution of semiconducting nanotubes in the samples. Trench scans are repeated three times using laser photon energies  $E_{ex} = 1.46, 1.59, \text{ and } 1.75 \text{ eV}$  to locate nanotubes with different  $S_{22}$  resonances. The results of the scans are carefully compared to verify that the same nanotube is only counted once and chiralities are assigned by performing PLE measurements. The chirality distribution is obtained by counting the number of nanotubes, and the results are plotted in Fig. 5.5e as a function of nanotube diameter

and chiral angle. It is clear that the nanotubes with larger chiral angles show larger population, in agreement with reports of chirality-dependent growth rates [61, 80–84]. This result is not dependent on physical parameters such as PL quantum yield [81, 82] or Raman scattering cross section [84], although PL measurements can only detect semiconducting nanotubes and the spectral range is limited by the capabilities of our laser and detector.

## 5.5 Raman Scattering

### 5.5.1 G-band and Resonance Features

The Raman scattering and PL can be measured simultaneously from an air-suspended SWCNT after the assignment of chirality by PLE mapping as described in the previous section. An example of Raman scattering from (9, 7) SWCNT is shown in Fig. 5.6 (top spectrum). The SWCNT was grown on Si pillars. The PLE mapping similar to the previous section was performed in order to identify the chirality [85] as in Fig. 5.6b. The clear single RBM and G mode features are obtained. Since these spectra are measured under the water vapor pressure of  $2.67 \times 10^3$  Pa, RBM frequency is blue shifted about  $7 \text{ cm}^{-1}$ , and PL emission wavelength is red shifted about 35 nm [85]. The Raman spectrum of (9, 7) SWCNT is compared with isolated SWCNT on  $\text{SiO}_2$  substrate which were transferred from horizontally aligned SWCNTs on a crystal quartz substrate [86]. Because of the aligned growth, most of SWCNTs are free from bundling or crossing. Except for the environmental effects of  $\text{SiO}_2$  and adsorbed water, pristine features of individual SWCNTs can be expected. The bottom Raman spectrum in Fig. 5.6a is from random and bulk SWCNTs grown on catalysts supported by zeolite particles [87]. In addition to the broad range of chirality distribution, certain broadening of each peak causes the complexity of interpretation of Raman peaks.

The G-band originates from an in-plane stretching mode of carbon-carbon bonds in graphitic materials [88]. For graphite, since the G-band comes from phonons with  $E_{2g}$  symmetry, which are equivalent longitudinal and transverse optical phonons at  $\Gamma$  point, the G-band appears as only one peak around  $1580 \text{ cm}^{-1}$ . In the contrast to the graphite or graphene, the G-band from SWCNTs appear around  $1590 \text{ cm}^{-1}$  as multiple peaks [89]. The G-band of SWCNTs composed of multiple peaks was explained to be the superposition of peaks from phonons with different symmetry, such as  $2A$ ,  $2E_1$  and  $2E_2$  modes [89]. Even more complex G-band is often discussed from bundled SWCNT samples. Especially, two most prominent peaks among the G-band are named  $G^+$  and  $G^-$  peaks. Here, lower and higher frequency peaks are defined as  $G^-$  and  $G^+$ , respectively. The discussion was not straightforward for bulk sample as in the bottom spectrum in Fig. 5.6a. Raman scattering spectra from individual semiconductor SWCNT in Fig. 5.6 are quite simple. There are only symmetric  $G^+$  and

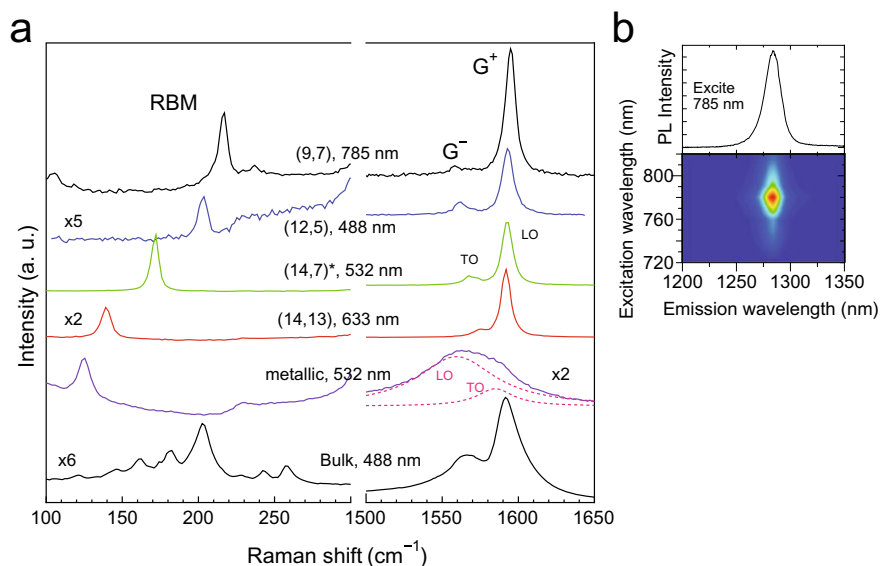


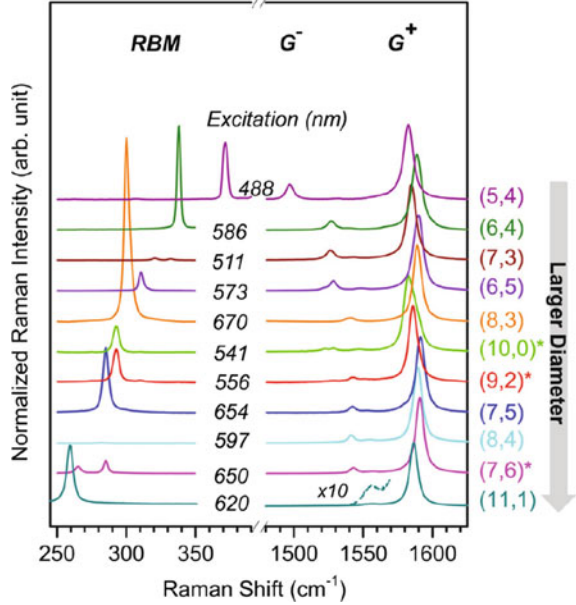
**Fig. 5.6** **a** Raman scattering from a suspended (9, 7) SWCNT compared with various individual SWCNT on SiO<sub>2</sub> substrates and bulk SWCNTs. **b** PL of (9,7) SWCNT simultaneously measured with Raman scattering. The (9, 7) SWCNT is kept in water vapor at  $2.67 \times 10^3$  Pa. The excitation laser was 785 nm. The PLE map in (b) is measured for the identification of chirality as in [85]. Original data are courtesy of Prof. Shohei Chiashi at UTokyo. Original Raman spectra for individual SWCNT on SiO<sub>2</sub> substrate transferred from horizontally aligned samples on crystal quartz are from [86]. Chirality of SWCNTs on SiO<sub>2</sub> substrate are determined by Kataura plot and systematic changes in the ratio of intensities of RBM peaks and G-band as in [86]. The assignments of (14, 7)\* is hence tentative. Raman spectrum for metallic SWCNT was averaged along a SWCNT. Here, dotted lines LO and TO are obtained by the decomposition of G-band by 2 Lorentzian functions. The bulk SWCNTs is grown by alcohol catalytic CVD technique in [87]

small G<sup>-</sup> peaks. The features are common to dispersed and chirality sorted nanotubes in solution [90] and previous suspended SWCNTs in air [91].

Raman spectra of chirality sorted semiconductor SWCNT are shown in Fig. 5.7 from [92]. Just like air-suspended SWCNT as in Fig. 5.6, G-band of single chirality semiconductor SWCNT exhibits only G<sup>+</sup> and G<sup>-</sup> peaks [93]. Because the theory states that the intensity of A mode peaks are strong [94], the G<sup>+</sup> and G<sup>-</sup> are usually assigned to A symmetry phonons. The feature of G<sup>+</sup> and G<sup>-</sup> peaks from individual or chirality sorted SWCNTs in solution are investigated in detail and it is found that the intensity ratio between RBM, G<sup>+</sup> and G<sup>-</sup> peaks depend on both  $d_{\text{tube}}$  and the chiral angle [92].

In the case of semiconducting SWCNTs, the G<sup>+</sup> and G<sup>-</sup> peaks, which originate from LO and TO phonons at the  $\Gamma$  point respectively, are quite sharp. The Raman shift of the G<sup>+</sup> peak ( $\omega_{G^+}$ ) (LO) does not depend on the tube diameter ( $d_t$ ) because the curvature effect is relatively small for longitudinal phonons. On the other hand, that of the G<sup>-</sup> peak ( $\omega_{G^-}$ ) (TO) clearly depends on the tube diameter due to the curvature

**Fig. 5.7**  $G^+$ ,  $G^-$  and RBM peaks of chirality sorted semiconducting SWCNTs. reproduced from [92] with permission of Copyright 2016, American Chemical Society



effect [95]. Therefore, the difference of their Raman shift ( $\omega_{G^+} - \omega_{G^-}$ ) is roughly expressed by the tube diameter ( $\omega_{G^+} - \omega_{G^-} = C_S/d_t^2$ ,  $C_S = 47.7 \text{ cm}^{-1} \text{ nm}^2$ ) [96]. In detail,  $\omega_{G^-}$  depends on both the diameter and chiral angle [97], as shown in Fig. 5.7.

For metallic SWCNTs, sharp  $G^+$  and broad  $G^-$  peaks are observed and they correspond to TO and LO phonons at the  $\Gamma$  point, respectively. Note that earlier references described the  $G^+$  and  $G^-$  peaks correspond to LO and TO phonons even for metallic SWCNTs. The LO phonon of metallic SWCNTs is softened due to Kohn anomaly [98], and the redshifted and broad (asymmetric)  $G^-$  peak of metallic SWCNTs is also called Breit-Wigner-Fano (BWF) peak [99]. Because of the Kohn anomaly, the G-band of metallic SWCNTs is drastically modulated by changing the Fermi energy [98, 100–102].

The density of states of SWCNTs exhibits almost discrete energy levels due to van Hove singularity and their optical transition energy ( $E_{ii}$ ) corresponds to the energy gap between two energy states. Raman scattering spectra from SWCNTs can be strongly enhanced with resonance excitation. If  $E_{ii}$  is equal to the energy of incident light ( $E_{\text{ex}}$ , incident resonance) or that of the scattered light ( $E_{\text{ex}} \pm E_{\text{phonon}}$ , scattered resonance), Raman scattering intensity will be significantly boosted. Here, a Raman process with  $E_{\text{ex}} + E_{\text{phonon}}$  and  $E_{\text{ex}} - E_{\text{phonon}}$  corresponds to anti-Stokes and Stokes scattering, respectively. Resonance Raman effect [103] is expressed by

$$I(E_{\text{ex}}) \propto \left| \frac{1}{(E_{\text{ex}} - E_{ii} + i\Gamma)(E_{\text{ex}} \pm E_{\text{phonon}} - E_{ii} + i\Gamma)} \right|^2 \quad (5.2)$$

where  $\Gamma$  is a resonance window.  $\Gamma$  is a damping constant and is related to the finite lifetime of the intermediate state. In Raman excitation profiles of the G-band, two resonance peaks, which correspond to the incident and scattered resonances, clearly appear with  $\Gamma = 26 - 43$  meV [104] for chirality separated SWCNT.

### 5.5.2 RBM Peaks

RBM peaks appear in the lower wavenumber region. Raman shift of RBM peaks ( $\omega_{\text{RBM}}$ ) is inversely proportional to the SWCNT diameter  $d_t$  [105, 106] as follows,

$$\omega_{\text{RBM}} = A/d_t. \quad (5.3)$$

Therefore, RBM peaks are often used to analyze the diameter distribution of SWCNT samples. However,  $\omega_{\text{RBM}}$  is not exactly expressed by (3), because of the environmental effects on  $\omega_{\text{RBM}}$ . Considering the environmental effect, the following equation,

$$\omega_{\text{RBM}} = A/d_t + B \quad (5.4)$$

is often used. This simple equation is useful for analysis of the SWCNT diameter, although the values of  $A$  and  $B$  vary depending on the environment. A discussion of more sophisticated dependence incorporating the environmental effect can be found in [107].

RBM peaks are strongly enhanced by resonance Raman effect and the resonance Raman effect is also expressed by Eq. (5.2). Spectra of RBM peaks of bulk sample change with the excitation wavelength. Each peak comes from different chirality and the intensity also clearly depends on the chirality. In general, SWCNTs with smaller chiral angle (near zigzag) exhibit stronger intensity for the RBM peaks [108]. Additionally, the relationship between the intensity of  $G^+$  and RBM peaks is investigated for chirality separated SWCNT samples and it shows chirality dependence [92].

### 5.5.3 Kataura Plot

As mentioned above, the intensity of RBM peaks is strongly enhanced by resonance Raman scattering effect. The phonon energy of RBM peaks is approximately a few tens of meV. When  $E_{\text{ex}}$  is in the visible or near infrared range,  $E_{\text{phonon}}$  of RBM peaks is quite small compared with  $E_{\text{ex}}$ . Therefore, it is usually impossible to distinguish the incident and scattered resonances in Eq. (5.2) and only  $E_{ii}$  is simply regarded as the resonance energy in RBM peaks. The relationship between  $\omega_{\text{RBM}}$  and  $E_{ii}$  is called the Kataura plot [4]. Figure 5.8 shows an example of Kataura plot, which is a compilation of experimental data [13, 84, 109–113]. Because both  $\omega_{\text{RBM}}$  [105, 106] and  $E_{ii}$  [114] are roughly proportional to  $1/d_t$ , the plots in Fig. 5.8 appear along lines from the lower

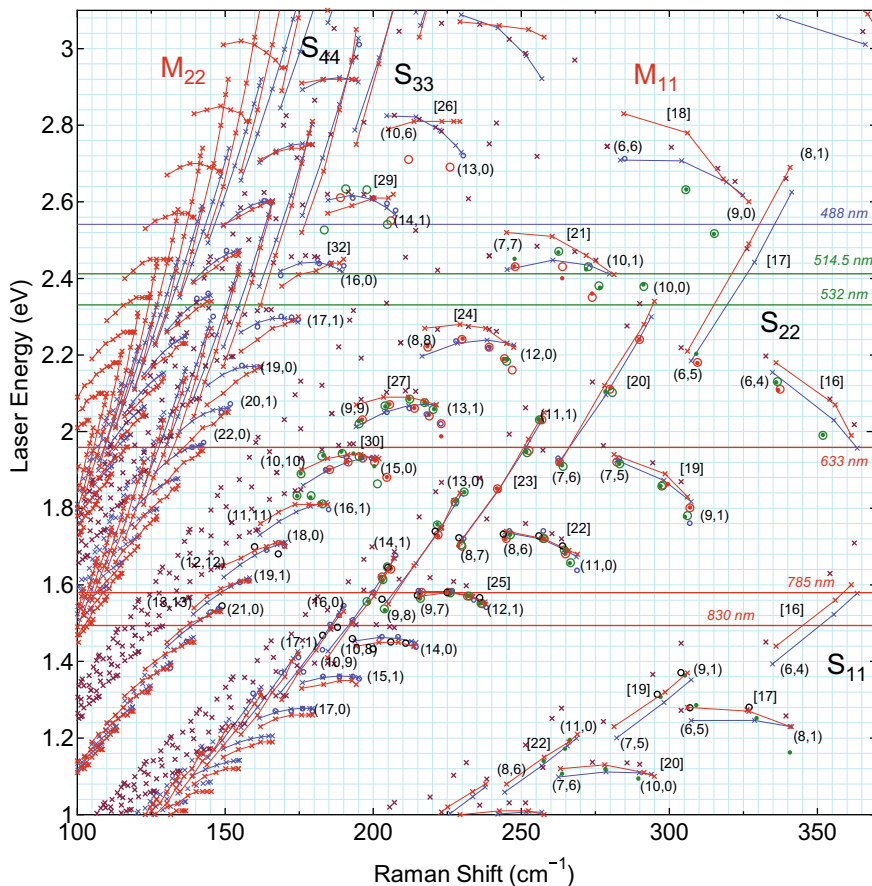


**Fig. 5.8** Empirical Kataura plots of SWCNTs. Blue open circles and blue cross marks connected with blue lines ( $S_{11}$ ,  $S_{22}$ ,  $M_{11}$ ,  $S_{33}$ ,  $S_{44}$ ) are measured and empirical formula, respectively, from Araujo et al. [110]. Red cross marks connected with red lines ( $S_{11}$ ,  $S_{22}$ ,  $M_{11}$ ,  $S_{33}$ ,  $S_{44}$ ,  $M_{22}$ ) are from nanotube atlas by Liu et al. [13] with (A, B) in Eq. (5.4) set as (217.8, 15.7). Brown cross marks are calculated from Araujo et al. [113]. Green open circles from Telg et al. [111], red open circles from Fantini et al. [109] and red solid circle from Jorio et al. [84] are measured from dispersed SWCNTs in solution. Green solid circles are measured from suspended SWCNTs from Michel et al. [112]. Chiral index ( $n, m$ ) and family pattern branches  $[2n+m]$  are indicated

left to the top right. Here, the  $S_{ii}$  and  $M_{ii}$  are the  $i$ -th optical transition energy of semiconducting and metallic SWCNTs, respectively. In Fig. 5.8, 6 different optical transition energies are shown, such as  $S_{44}$ . Because  $E_{ii}$  depends on both  $d_i$  and the chiral angle ( $\theta$ ), the plots do not appear just along the lines and are slightly spread. In Fig. 5.8, the plots with the same value of  $2n+m$  are connected with line segments and they show the so-called “family pattern” [115]. In Fig. 5.8, some of plots are denoted with chiral index ( $n, m$ ) and some of branches of family pattern are denoted with  $[2n+m]$ . As mentioned in Sect. 5.2, semiconducting SWCNTs with  $(2n + m) \bmod 3 =$

1 and 2 are called ‘type-I’ (‘SI’ or ‘mod 2’) and ‘type-II’ (‘SII’ or ‘mod 1’) SWCNTs, respectively. As an example, (7, 5) SWCNT schematically shown in Figs. 5.1 and 5.2a is type I ( $2n+m=19$ ). As shown in Fig. 5.2a, a cutting line corresponding to  $S_{11}$ ,  $S_{22}$  for type I SWCNT locate in  $\Gamma$  and M direction, respectively. The direction is opposite for type II. Because the slope of valence-conduction energy gap near K point is sharper in  $\Gamma$  direction than M direction,  $S_{11}$  branches spread to larger energy side for type I and smaller energy side for type II. For  $S_{22}$ , the spread direction is opposite. Some other properties of SWCNTs show type-dependence. For example,  $E_{ii}$  depends on strain and whether  $E_{ii}$  increases or decreases is determined by the type [116].

As shown in Fig. 5.8, the empirical Kataura plot proposed by Araujo et al. (2007) [110] match reasonably well with experimental resonant Raman data obtained from micelle-suspended samples by Telg et al. [111], Fantini et al. [109], and Jorio et al. [84]. The air-suspended SWCNTs data from Michel et al. [112] also reasonably agree with the empirical Kataura plot. This is rather surprising because the original SWCNT sample used by Araujo et al. [110] was vertically aligned SWCNT forest [49]. Later, we understand that randomly-oriented, less-bundled, and small diameter SWCNTs suspended in the forest are responsible to resonant Raman signals. The empirical equation in atlas of carbon nanotubes in Liu et al. [13] is also compared in Fig. 5.8. Here, the Raman shift was estimated with the same relation as Araujo et al. [110]. Both empirical relations agree well with slight deviations for  $S_{33}$  and  $S_{44}$ . Resonant Raman measurements of relatively large diameter and chirality assigned SWCNT are essential to verify which relation is more suitable for better Kataura plot for  $S_{33}$  and  $S_{44}$ . As in Chiashi et al. [85], by fully removing water absorption on SWCNTs, a considerable red-shift of Raman frequency is observed. The empirical Kataura plot proposed by Araujo et al. [113] using the Eq. (3) is known to fit better for vacuum condition [107].

Based on the accurate Kataura plot, it is possible to assign the chirality from measured RBM peaks. When  $E_{ii}$  is close to the  $E_{ex}$ , the RBM peaks are observed. The resonance window ( $\Gamma$ ) depend on SWCNT samples, such as SDS wrapped SWCNTs in solution ( $\Gamma = 60\text{meV}$ ) and bundled SWCNTs ( $\Gamma = 120\text{meV}$ ) [109]. According to Kataura plots, RBM peaks of bulk sample can be roughly assigned. For example, RBM peak around  $200\text{cm}^{-1}$  and around  $250\text{cm}^{-1}$  in Fig. 5.6a (bottom spectrum) corresponds to semiconducting SWCNTs with  $2n + m = 29$  and metallic SWCNTs with  $2n + m = 21$ , respectively.

## 5.6 Recent Advances

### 5.6.1 Inter-Tube Coupling in Double-Walled Carbon Nanotubes

DWCNTs consist of two coaxially aligned SWCNTs, in which the wall can be either semiconducting or metallic depending on its chiral index. However, properties of

DWCNTs are not just a superposition of those of the constituent SWCNTs but can be strongly modulated by (i) interlayer van der Waals mechanical and electronic interactions, mainly depending on the wall-to-wall distance [117–120] and (ii) Moiré interference, mainly depending on the relative chiral angles [121–123]. Early theory predicted that strong wavefunction mixing within two commensurate semiconducting walls could even induce a semiconductor-to-metal transition [124]. However, commensurate DWCNTs have never been observed experimentally because it is almost impossible to have two commensurate SWCNTs with the radius difference matching the tube-tube separation in a DWCNT.

Especially, the interlayer interaction of incommensurate DWCNTs is indicated by the emergence of new and/or collective shifted optical modes in the Raman spectrum [117–120] the modification in the emission PL [125] and significant shifts (–50 to 200 meV) of optical transitions in the absorption spectrum [117]. These experimental findings are also supported by theoretical results that electron wavefunctions between incommensurate inner and outer-wall nanotubes can also hybridize and even weak van der Waals interlayer coupling in incommensurate DWCNTs can slightly change the band structure of pristine SWCNTs [121].

In contrast to the weak-coupling cases, a strong-coupling effect in a structure-identified 1D Moiré superlattice is also experimentally observed and identified [122]. A drastic change of the optical transition in Rayleigh scattering spectrum is found in a DWCNT with chirality (12,11) @ (17,16). The marked change originated from the strong inter-tube coupling effect in the Moiré superlattice formed by two nearly armchair nanotubes, which remarkably changes the electronic band structure and selection rules of optical absorption from the simple sum of the constituent pristine nanotubes [123]. This observation provides valuable insights on inter-tube coupling and may lead to an extended exploration of rich Moiré physics in 1D structures such as strongly correlated physics, Moiré excitons, and superconductivity.

### 5.6.2 *Hetero-Nanotubes*

In addition to DWCNTs, SWCNTs can be coaxially surrounded by hBN nanotubes and transition metal dichalcogenides (TMD) nanotubes. Those hetero-nanotubes based on SWCNTs will provide excitingly rich spectroscopy data. A new coaxial nanotube structure has been synthesized, in which a mono- or few-layer hexagonal boron nitride nanotube (BNNT) seamlessly wraps around a SWCNT; SWCNT@BNNT [126]. These nanotubes are named as 1D van der Waals hetero-nanotubes, because no correlation between the chiral angle of inner SWCNT and outer BNNT for ‘double-walled’ SWCNT@BNNT were found. We have further developed the 1D coating CVD of transition metal dichalcogenide nanotubes (TMD-NT), such as MoS<sub>2</sub> nanotubes [126]. As shown in Fig. 5.9, these nanotubes can be labeled as SWCNT@BNNT@MoS<sub>2</sub>. SWCNT from SWCNT@BNNT can be removed by a gentle oxidation process because BNNTs are thermally more stable than SWCNTs. Hence, the inner diameter of produced BNNTs could be determined by the original

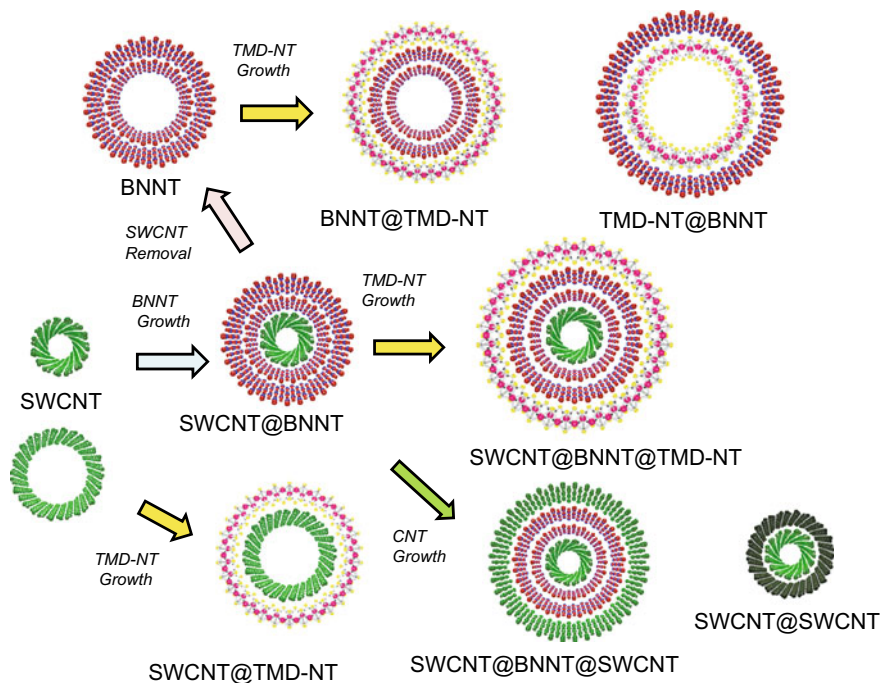


**Fig. 5.9** Various structures of hetero-nanotubes

SWCNTs. Subsequent  $\text{MoS}_2$  CVD leads to  $\text{BNNT@MoS}_2$ . The hetero-nanotubes are further characterized by HR-TEM, STEM-EELS, absorption, Raman, and PL spectroscopy (a bright PL for  $\text{BNNT@MoS}_2$ ). From DFT calculations, the 2D  $\text{MoS}_2$  K point direct band gap is expected in  $\text{MoS}_2$  nanotubes with a larger diameter such as 5 nm. For the hetero-nanotube  $\text{SWCNT@BNNT@MoS}_2$ , the PL from  $\text{MoS}_2$  was quenched by inner SWCNT (metallic or small band gap semiconductor). The electronic and phononic structures are expected to be modulated by inter-tube coupling. The inter-tube exciton can also be expected by choosing appropriate semiconductor SWCNT and TMD-NT.

### 5.6.3 Luttinger-Liquid Plasmon

Quantum-confined electrons in SWCNTs behave as a Luttinger liquid, a strongly correlated electronic matter distinctly different from the quasi-free electrons described by the Fermi liquid [127, 128]. Many electrical transport and photoemission measurements have shown the presence of Luttinger liquid in SWCNTs [129]. Due to this strong quantum confinement, Luttinger-liquid plasmons in SWCNTs with a diameter of 1 nm should persist to visible frequencies before the first intersubband transition

appearing. Besides, the forbidden backscattering of Dirac electrons, evidenced by ballistic transport up to micrometer lengths in metallic SWCNTs, can lead to strongly confined but low-loss Luttinger-liquid plasmons.

Recently, the first reported optical observation of Luttinger-liquid plasmons in SWCNTs using infrared scattering-type scanning nearfield optical microscopy (s-SNOM) [130] shows that a Luttinger liquid of 1D Dirac electrons in carbon nanotubes exhibits quantum plasmons which behave qualitatively differently from classical plasmon excitations. The Luttinger-liquid plasmons propagate at ‘quantized’ velocities that are independent of carrier concentration or excitation wavelength and simultaneously exhibit extraordinary spatial confinement and high quality factor. Following the observation of linear Luttinger-liquid in carbon nanotubes, nonlinear Luttinger-liquid of semiconducting SWCNTs was experimentally explored [131]. With carrier density controlled by electrostatic gating, in situ infrared nano-imaging results have shown that plasmon wavelength, amplitude, and quality factor in semiconducting SWCNTs can be continuously tuned due to the nonlinear band dispersion. In addition, both the propagation velocity and the dynamic damping of plasmons can be fine-tuned, which is well captured by the nonlinear Luttinger liquid theory. Such Luttinger-liquid plasmons could enable novel low-loss plasmonic circuits for the subwavelength manipulation of light.

#### 5.6.4 *Coupling to Photonic Structures*

Advances in silicon photonics have been expanding the capabilities of monolithic photonic circuits, and the integration of nanoscale emitters would allow for further scaling and increased functionality. In this regard, CNTs are promising because they can be directly synthesized on silicon [132] and they are telecom-band emitters [25, 32] that do not suffer from absorption loss by silicon. Furthermore, nanotube emitters operate at room temperature and they can be electrically driven [27, 30, 133–135].

To utilize such characteristics in monolithic optical circuits, coupling to photonic structures is essential. Microcavities, in particular, offer quantum electrodynamical effects for increased performance and functionality by confining electric fields into a small mode volume. Exciton polaritons can form when nanotube emission is strongly coupled to a cavity [136], whereas the interaction of CNTs with cavities results in an increased spontaneous emission rate in the weak-coupling regime [11, 137–140].

Here PL from individual CNTs are coupled to silicon photonic crystal nanobeam cavities with ultralow mode volumes [11]. The excellent optical properties of as-grown air-suspended CNTs [30, 141–143] are utilized, and they are integrated with specially designed cavities with large fields in the air, distinctly different from the standard dielectric-mode cavities [144–148]. The fabricated devices are shown as a schematic in Fig. 5.10a. Catalyst particles are placed across a trench from the cavity, and chemical vapor deposition is performed to grow CNTs onto the cavities [138]. An electron micrograph of a device after nanotube growth is shown in Fig. 5.10b.

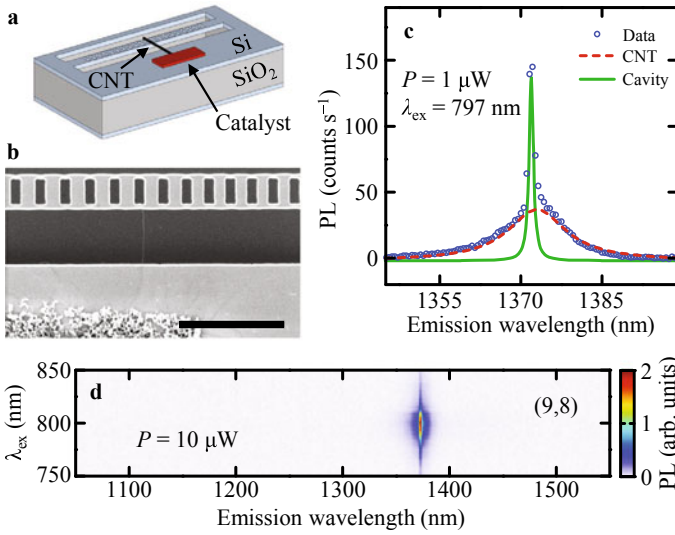


**Fig. 5.10** An individual CNT coupled to a nanobeam cavity. **a** A schematic of a device. **b** Scanning electron microscope image of a device with a suspended nanotube. Scale bar is 2  $\mu\text{m}$ . **c** Typical PL spectrum of an air-mode device coupled to a nanotube. The dots are data and the lines are Lorentzian fits. **d** PLE map of the device shown in (c) taken with  $P = 10 \mu\text{W}$  and the laser polarization perpendicular to the nanobeam. Original data presented in [11]

In Fig. 5.10c, a PL spectrum from one of such devices taken with an excitation power  $P = 1 \mu\text{W}$  and an excitation wavelength  $\lambda_{\text{ex}} = 797 \text{ nm}$  is shown. On top of the broad direct emission from the nanotube, there is a very sharp peak which is the cavity mode, indicating that the nanotube emission is optically coupled to the cavity. To further characterize the device, PLE spectroscopy is performed (Fig. 5.10d). A single peak is observed in the PLE map, demonstrating an isolated single nanotube. Using tabulated data [34], the chirality is determined to be (9,8). The intensity of the sharp cavity mode is maximized at the same wavelength as the  $E_{22}$  resonance of this tube, showing that the absorption originates from the nanotube and that the cavity mode is excited by the nanotube emission.

These results demonstrate the feasibility of integrating telecom-wavelength nanotube emitters in silicon photonics, opening up further possibilities for scaling down monolithic photonic circuits. By interfacing the cavities with waveguides, photons emitted from the nanotubes can be guided over the chip and to external components such as optical fibers. The nanophotonic structure also allows us to take advantage of quantum electrodynamical effects, where the acceleration of the emission rate would increase the quantum efficiency.

## 5.7 Summary

In summary, we have described the unique optical properties of individual SWCNTs. SWCNTs host strongly bound 1D excitons, whose transition energies are inversely proportional to the CNT diameter and can be further tuned in different dielectric environments. Such transitions and their radiative decay can be probed by Raman scattering, light absorption, PL or Rayleigh scattering. Inter-tube coupling in Double-walled carbon nanotubes or hetero-nanotube has been explored. Furthermore, photonic structures have been coupled with a tube for further scaling and increased functionality. However, this is only the beginning of the study and of the application of nanotube photonics. As the production of pure CNTs advances, we expect to see applications in electrically pumped solid-state nanoscale light sources and lasers, CNT light guides and nonlinear devices.

**Acknowledgements** The authors thank Prof. Shohei Chiashi, Prof. Rong Xiang & Prof. Keigo Otsuka at the University of Tokyo, Prof. Taiki Inoue at Osaka University, and Prof. Yuhei Miyauchi at Kyoto University for discussions and for offering the original data. Part of this work was supported by JSPS KAKENHI Grant Numbers JP18H05329, JP20H00220, JP20H02558 and by JST, CREST Grant Number JPMJCR20B5, Japan as well as MIC (SCOPE 191503001). Kahui Liu acknowledged the supports from the National Natural Science Foundation of China (52025023, 51991340, and 51991342) and Beijing Natural Science Foundation (JQ19004)

## References

1. S. Iijima, *Nature* **354**, 56–58 (1991)
2. S. Iijima, T. Ichihashi, *Nature* **363**, 603–605 (1993)
3. A.M. Rao, E. Richter, S. Bandow, B. Chase, P.C. Eklund, K.A. Williams, S. Fang, K.R. Subbaswamy, M. Menon, A. Thess, R.E. Smalley, G. Dresselhaus, M.S. Dresselhaus, *Science* **275**, 187–191 (1997)
4. H. Kataura, Y. Kumazawa, Y. Maniwa, I. Umezū, S. Suzuki, Y. Ohtsuka, Y. Achiba, *Synth. Met.* **103**, 2555–2558 (1999)
5. A. Jorio, R. Saito, J.H. Hafner, C.M. Lieber, M. Hunter, T. McClure, G. Dresselhaus, M.S. Dresselhaus, *Phys. Rev. Lett.* **86**, 1118–1121 (2001)
6. S.M. Bachilo, M.B. Strano, C. Kittrell, R.H. Hauge, R.E. Smalley, R.B. Weisman, *Science* **298**, 2361–2366 (2002)
7. M.S. Arnold, A.A. Green, J.F. Hulvat, S.I. Stupp, M.C. Hersam, *Nat. Nanotechnol.* **1**, 60–65 (2006)
8. X. Tu, S. Manohar, A. Jagota, M. Zheng, *Nature* **460**, 250–253 (2009)
9. H. Liu, D. Nishide, T. Tanaka, H. Kataura, *Nat. Commun.* **2**, 1–8 (2011)
10. J. Lefebvre, Y. Homma, P. Finnie, *Phys. Rev. Lett.* **90**, 217401 (2003)
11. R. Miura, S. Imamura, R. Ohta, A. Ishii, X. Liu, T. Shimada, S. Iwamoto, Y. Arakawa, Y.K. Kato, *Nat. Commun.* **5**, 5580 (2014)
12. F. Wang, M.Y. Sfeir, L. Huang, X.M. Huang, Y. Wu, J. Kim, J. Hone, S. O'Brien, L.E. Brus, T.F. Heinz, *Phys. Rev. Lett.* **96**, 167401 (2006)
13. K. Liu, J. Deslippe, F. Xiao, R.B. Capaz, X. Hong, S. Aloni, A. Zettl, W. Wang, X. Bai, S.G. Louie, E. Wang, F. Wang, *Nat. Nanotechnol.* **7**, 325–329 (2012)
14. S. Reich, C. Thomsen, J. Maultzsch, *Carbon Nanotubes: Basic Concepts and Physical Properties* (Wiley-VCH, Weinheim, Germany, 2004)

15. R. Saito, G. Dresselhaus, M.S. Dresselhaus, *Physical Properties of Carbon Nanotubes* (Imperial College Press, London, 1998)
16. F. Wang, G. Dukovic, L.E. Brus, T.F. Heinz, *Science* **308**, 838–841 (2005)
17. J. Lefebvre, P. Finnie, *Nano Lett.* **8**, 1890–1895 (2008)
18. Y. Toyozawa, *Optical Processes in Solids* (Cambridge Univ. Press, 2003)
19. T. Ando, *J. Phys. Soc. Jpn.* **66**, 1066–1073 (1997)
20. K.H. Liu, X.P. Hong, S. Choi, C.H. Jin, R.B. Capaz, J. Kim, W.L. Wang, X.D. Bai, S.G. Louie, E.G. Wang, F. Wang, *P. Natl. Acad. Sci.* **111**, 7564–7569 (2014)
21. J.-C. Blancon, M. Paillet, H.N. Tran, X.T. Than, S.A. Guebrou, A. Ayari, A.S. Miguel, N.-M. Phan, A.-A. Zahab, J.-L. Sauvajol, N.D. Fatti, F. Vallée, *Nat. Commun.* **4**, 2542 (2013)
22. M.Y. Sfeir, F. Wang, L.M. Huang, C.C. Chuang, J. Hone, S.P. O’Brien, T.F. Heinz, L.E. Brus, *Science* **306**, 1540–1543 (2004)
23. M.Y. Sfeir, T. Beetz, F. Wang, L.M. Huang, X.M.H. Huang, M.Y. Huang, J. Hone, S. O’Brien, J.A. Misewich, T.F. Heinz, L.J. Wu, Y.M. Zhu, L.E. Brus, *Science* **312**, 554–556 (2006)
24. M.S. Dresselhaus, G. Dresselhaus, R. Saito, A. Jorio, *Phys. Rep.* **409**, 47–99 (2005)
25. M.J. O’Connell, S.M. Bachilo, C.B. Huffman, V.C. Moore, M.S. Strano, E.H. Haroz, K.L. Rialon, P.J. Boul. W.H. Noon, C. Kittrell, J.P. Ma, R.H. Hauge, R.B. Weisman, R.E. Smalley, *Science* **297**, 593–596 (2002)
26. M. Freitag, Y. Martin, J.A. Misewich, R. Martel, P.H. Avouris, *Nano Lett.* **3**, 1067–1071 (2003)
27. J. Chen, V. Perebeinos, M. Freitag, J. Tsang, Q. Fu, J. Liu, P. Avouris, *Science* **310**, 1171–1174 (2005)
28. V.V. Didenko, V.C. Moore, D.S. Baskin, R.E. Smalley, *Nano Lett.* **5**, 1563–1567 (2005)
29. J. Lefebvre, P. Finnie, *Phys. Rev. Lett.* **98**, 167406 (2007)
30. D. Mann, Y.K. Kato, A. Kinkhabwala, E. Pop, J. Cao, X. Wang, L. Zhang, Q. Wang, J. Guo, H. Dai, *Nat. Nanotechnol.* **2**, 33–38 (2007)
31. N.M. Gabor, Z. Zhong, K. Bosnick, J. Park, P.L. McEuen, *Science* **325**, 1367–1371 (2009)
32. R.B. Weisman, S.M. Bachilo, *Nano Lett.* **3**, 1235 (2003)
33. J. Lefebvre, J.M. Fraser, Y. Homma, P. Finnie, *Appl. Phys. A* **78**, 1107 (2004)
34. Y. Ohno, S. Iwasaki, Y. Murakami, S. Kishimoto, S. Maruyama, T. Mizutani, *Phys. Rev. B* **73**, 235427 (2006)
35. S. Chiashi, S. Watanabe, T. Hanashima, Y. Homma, *Nano Lett.* **8**, 3097 (2008)
36. C.F. Bohren, D.R. Huffman, *Absorption and Scattering of Light by Small Particles* (John Wiley & Sons, 2008)
37. Z.H. Yu, L. Brus, *J. Phys. Chem. B* **105**, 1123–1134 (2001)
38. E. Malic, M. Hirtschulz, F. Milde, Y. Wu, J. Maultzsch, T.F. Heinz, A. Knorr, S. Reich, *Phys. Rev. B* **77**, 045432 (2008)
39. H. Zeng, H. Zhao, F.C. Zhang, X. Cui, *Phys. Rev. Lett.* **102**, 136406 (2009)
40. D.Y. Joh, L.H. Herman, S.Y. Ju, J. Kinder, M.A. Segal, J.N. Johnson, G.K. Chan, J. Park, *Nano Lett.* **11**, 1–7 (2011)
41. J. Lefebvre, P. Finnie, *Nano Res.* **4**, 788–794 (2011)
42. W. Wu, J. Yue, X. Lin, D. Li, F. Zhu, X. Yin, J. Zhu, J. Wang, J. Zhang, Y. Chen, X. Wang, T. Li, Y. He, X. Dai, P. Liu, Y. Wei, J. Wang, W. Zhang, Y. Huang, L. Fan, L. Zhang, Q. Li, S. Fan, K. Jiang, *Nano Res.* **8**, 2721–2732 (2015)
43. F. Yang, X. Wang, D. Zhang, J. Yang, D. Luo, Z. Xu, J. Wei, J.-Q. Wang, Z. Xu, F. Peng, X. Li, R. Li, Y. Li, M. Li, X. Bai, F. Ding, Y. Li, *Nature* **510**, 522–524 (2014)
44. S. Zhang, L. Kang, X. Wang, L. Tong, L. Yang, Z. Wang, K. Qi, S. Deng, Q. Li, X. Bai, F. Ding, *J. Zhang, Nature* **543**, 234–238 (2017)
45. Y.X. Bai, R.F. Zhang, X. Ye, Z.X. Zhu, H.H. Xie, B.Y. Shen, D.L. Cai, B.F. Liu, C.X. Zhang, Z. Jia, S.L. Zhang, X.D. Li, F. Wei, *Nat. Nanotechnol.* **13**, 589–595 (2018)
46. D. Christofilos, J.C. Blancon, J. Arvanitidis, A.S. Miguel, A. Ayari, N. Del Fatti, F. Vallée, *J. Phys. Chem. C* **3**, 1176–1181 (2012)
47. Y. Wu, M. Huang, F. Wang, X.H. Huang, S. Rosenblatt, L. Huang, H. Yan, S.P. O’Brien, J. Hone, T.F. Heinz, *Nano Lett.* **8**, 4158–4161 (2008)

48. M.F. Islam, D.E. Milkie, C.L. Kane, A.G. Yodh, J.M. Kikkawa, *Phys. Rev. Lett.* **93**, 037404 (2004)
49. Y. Murakami, E. Einarsson, T. Edamura, S. Maruyama, *Phys. Rev. Lett.* **94**, 087402 (2005)
50. Y. Miyauchi, M. Oba, S. Maruyama, *Phys. Rev. B* **74**, 205440 (2006)
51. F. Vialla, C. Roquelet, B. Langlois, G. Delport, S.M. Santos, E. Deleporte, P. Roussignol, C. Delalande, C. Voisin, J.-S. Lauret, *Phys. Rev. Lett.* **111**, 137402 (2013)
52. J.A. Fagan, C.Y. Khripin, C.A. Silvera Batista, J.R. Simpson, E.H. Hroz, A.R. Hight Walker, M. Zheng, *Adv. Mater.* **26**, 2800–2804 (2014)
53. Y. Yomogida, T. Tanaka, M. Zhang, M. Yudasaka, X. Wei, H. Kataura, *Nat. Commun.* **7**, 1–8 (2016)
54. G. Ao, C.Y. Khripin, M. Zheng, *J. Am. Chem. Soc.* **136**, 103183–10392 (2014)
55. Y. Ohno, S. Kishimoto, T. Mizutani, T. Okazaki, H. Shinohara, *Appl. Phys. Lett.* **84**, 1368–1370 (2004)
56. E.J. Lee, K. Balasubramanian, J. Dorfmler, R. Vogelgesang, N. Fu, A. Mews, M. Burghard, *Kern. Small* **3**, 2038–2042 (2007)
57. M. Barkelid, G.A. Steele, V. Zwiller, *Nano Lett.* **12**, 5649–5653 (2012)
58. M. Barkelid, V. Zwiller, *Nat. Photon.* **8**, 47–51 (2013)
59. S. Berciaud, L. Cognet, P. Poulin, R.B. Weisman, B. Lounis, *Nano Lett.* **7**, 1203–1207 (2007)
60. F. Wang, D.J. Cho, B. Kessler, J. Deslippe, P.J. Schuck, S.G. Louie, A. Zettl, T.F. Heinz, Y.R. Shen, *Phys. Rev. Lett.* **99**, 227401 (2007)
61. K. Liu, X. Hong, Q. Zhou, C. Jin, J. Li, W. Zhou, J. Liu, E. Wang, A. Zettl, F. Wang, *Nat. Nanotechnol.* **8**, 917–922 (2013)
62. L.H. Herman, C.J. Kim, Z.H. Wang, M.H. Jo, J. Park, *Appl. Phys. Lett.* **101**, 123102 (2012)
63. F. Yao, C. Liu, C. Chen, S. Zhang, Q. Zhao, F. Xiao, M. Wu, J. Li, P. Gao, J. Zhao, X. Bai, S. Maruyama, D. Yu, E. Wang, Z. Sun, J. Zhang, F. Wang, K. Liu, *Nat. Commun.* **9**, 3387 (2018)
64. H.B. Chu, R.L. Cui, J.Y. Wang, J.A. Yang, Y. Li, *Carbon* **49**, 1182–1188 (2011)
65. R. Zhang, Y. Zhang, Q. Zhang, H. Xie, H. Wang, J. Nie, Q. Wen, F. Wei, *Nat. Commun.* **4**, 1727–1735 (2013)
66. J. Wang, T. Li, B. Xia, X. Jin, H. Wei, W. Wu, Y. Wei, J. Wang, P. Liu, L. Zhang, *Nano Lett.* **14**, 3527–3533 (2014)
67. S. Chaudhary, J.H. Kim, K.V. Singh, M. Ozkan, *Nano Lett.* **4**, 2415–2419 (2004)
68. K. Balasubramanian, Y. Fan, M. Burghard, K. Kern, M. Friedrich, U. Wannek, A. Mews, *Appl. Phys. Lett.* **84**, 2400–2402 (2004)
69. A.W. Tsen, L.A. Donev, H. Kurt, L.H. Herman, J. Park, *Nat. Nanotechnol.* **4**, 108–113 (2009)
70. F. Wang, S. Wang, F. Yao, H. Xu, N. Wei, K. Liu, L.-M. Peng, *ACS Nano* **10**, 9595–9601 (2016)
71. Q. Zhao, F. Yao, Z. Wang, S. Deng, L. Tong, K. Liu, J. Zhang, *Adv. Mater.* **29**, 1701959 (2017)
72. A. Ishii, M. Yoshida, Y.K. Kato, *Phys. Rev. B* **91**, 125427 (2015)
73. S. Maruyama, R. Kojima, Y. Miyauchi, S. Chiashi, M. Kohno, *Chem. Phys. Lett.* **360**, 229 (2002)
74. L. Huang, X. Cui, B. White, S.P. O’Brien, *J. Phys. Chem. B* **108**, 16451 (2004)
75. P.H. Tan, A.G. Rozhin, T. Hasan, P. Hu, V. Scardaci, W.I. Milne, A.C. Ferrari, *Phys. Rev. Lett.* **99**, 137402 (2007)
76. L. Yang, M.P. Anantram, J. Han, J.P. Lu, *Phys. Rev. B* **60**, 13874 (1999)
77. M. Huang, Y. Wu, B. Chandra, H. Yan, Y. Shan, T.F. Heinz, J. Hone, *Phys. Rev. Lett.* **100**, 136803 (2008)
78. A. G. Souza Filho, N. Kobayashi, J. Jiang, A. Gr’uneis, R. Saito, S. B. Cronin, J. Mendes Filho, G. G. Samsonidze, G. Dresselhaus, M. S. Dresselhaus, *Phys. Rev. Lett.* **95**, 217403 (2005)
79. P. Koskinen, *Phys. Rev. B* **82**, 193409 (2010)
80. S. Bandow, S. Asaka, Y. Saito, A.M. Rao, L. Grigorian, E. Richter, P.C. Eklund, *Phys. Rev. Lett.* **80**, 3779 (1998)

81. S.M. Bachilo, L. Balzano, J.E. Herrera, F. Pompeo, D.E. Resasco, R.B. Weisman, J. Am. Chem. Soc. **125**, 11186 (2003)
82. Y. Miyauchi, S. Chiashi, Y. Murakami, Y. Hayashida, S. Maruyama, Chem. Phys. Lett. **387**, 198 (2004)
83. R. Rao, D. Liptak, T. Cherukuri, B.I. Yakobson, B. Maruyama, Nat. Mater. **11**, 213 (2012)
84. A. Jorio, C. Fantini, M.A. Pimenta, R.B. Capaz, G.G. Samsonidze, G. Dresselhaus, M.S. Dresselhaus, J. Jiang, N. Kobayashi, A. Grüneis, R. Saito, Phys. Rev. B **71**, 075401 (2005)
85. S. Chiashi, K. Kono, D. Matsumoto, J. Shitaba, N. Homma, A. Beniya, T. Yamamoto, Y. Homma, Phys. Rev. B **91**, 155415 (2015)
86. K. Otsuka, S. Yamamoto, T. Inoue, B. Koyano, H. Ukai, R. Yoshikawa, R. Xiang, S. Chiashi, S. Maruyama, ACS Nano **12**, 3994–4001 (2018)
87. B. Hou, C. Wu, T. Inoue, S. Chiashi, R. Xiang, S. Maruyama, Carbon **119**, 502–510 (2017)
88. F. Tuinstra, J.L. Koenig, J. Chem. Phys. **53**, 1126–1130 (1970)
89. A. Jorio, M.A. Pimenta, A.G. Souza, G.G. Samsonidze, A.K. Swan, M.S. Unlu, B.B. Goldberg, R. Saito, G. Dresselhaus, M.S. Dresselhaus, Phys. Rev. Lett. **90**, 107403 (2003)
90. S. Lebedkin, F. Hennrich, T. Skipa, M.M. Kappes, J. Phys. Chem. B **107**, 1949–1956 (2003)
91. Y. Kobayashi, T. Yamashita, Y. Ueno, O. Niwa, Y. Homma, T. Ogino, Chem. Phys. Lett. **386**, 153–157 (2004)
92. Y. Piao, J.R. Simpson, J.K. Streit, G. Ao, M. Zheng, J.A. Fagan, A.R.H. Walker, ACS Nano **10**, 5252–5259 (2016)
93. H.B. Son, Y. Hori, S.G. Chou, D. Nezich, G.G. Samsonidze, G. Dresselhaus, M.S. Dresselhaus, E.B. Barros, Appl. Phys. Lett. **85**, 4744–4746 (2004)
94. V. Avramenko, S.B. Rochal, Phys. Rev. B **87**, 035407 (2013)
95. X. Blase, L.X. Benedict, E.L. Shirley, S.G. Louie, Phys. Rev. Lett. **72**, 1878–1881 (1994)
96. A. Jorio, A.G. Souza, G. Dresselhaus, M.S. Dresselhaus, A.K. Swan, M.S. Unlu, B.B. Goldberg, M.A. Pimenta, J.H. Hafner, C.M. Lieber, R. Saito, Phys. Rev. B **65**, 155412 (2002)
97. H. Telg, J.G. Duque, M. Staiger, X. Tu, F. Hennrich, M.M. Kappes, M. Zheng, J. Maultzsch, C. Thomsen, S.K. Doorn, ACS Nano **6**, 904–911 (2012)
98. H. Farhat, H. Son, G. Samsonidze, S. Reich, M. Dresselhaus, J. Kong, Phys. Rev. Lett. **99**, 145506 (2007)
99. S.D.M. Brown, A. Jorio, P. Corio, M.S. Dresselhaus, G. Dresselhaus, R. Saito, K. Kneipp, Phys. Rev. B **63**, 155414 (2001)
100. J.S. Park, K. Sasaki, R. Saito, W. Izumida, M. Kalbac, H. Farhat, G. Dresselhaus, M.S. Dresselhaus, Phys. Rev. B **80**, 081402(R) (2009)
101. K. Nguyen, A. Gaur, M. Shim, Phys. Rev. Lett. **98**, 145504 (2007)
102. B. Hatting, S. Heeg, K. Ataka, J. Heberle, F. Hennrich, M.M. Kappes, R. Krupke, S. Reich, Phys. Rev. B **87**, 165442 (2013)
103. M.A. Pimenta, A. Marucci, S.A. Empedocles, M.G. Bawendi, E.B. Hanlon, A.M. Rao, P.C. Eklund, R.E. Smalley, G. Dresselhaus, M.S. Dresselhaus, Phys. Rev. B **58**, R16016–R16019 (1998)
104. J.G. Duque, H. Chen, A.K. Swan, A.P. Shreve, S. Kilina, S. Tretiak, X. Tu, M. Zheng, S.K. Doorn, ACS Nano **5**, 5233–5241 (2011)
105. G.D. Mahan, Phys. Rev. B **65**, 2354027 (2002)
106. V. Perebeinos, J. Tersoff, Phys. Rev. B **79**, 241409 (2009)
107. S. Chiashi, Y. Homma, S. Maruyama, Handbook of Carbon Nanomaterials **10**, 49–73 (2019)
108. J. Jiang, R. Saito, K. Sato, J.S. Park, G.G. Samsonidze, A. Jorio, G. Dresselhaus, M.S. Dresselhaus, Phys. Rev. B **75**, 035405 (2007)
109. C. Fantini, A. Jorio, M. Souza, M. S. Strano, M. S. Dresselhaus, and M. A. Pimenta, Phys. Rev. Lett. **93**, 147406, (2004)
110. P. T. Araujo, S. K. Doorn, S. Kilina, S. Tretiak, E. Einarsson, S. Maruyama, H. Chacham, M. A. Pimenta, A. Jorio, Phys. Rev. Lett. **98**, 067401, (2007)
111. H. Telg, J. Maultzsch, S. Reich, F. Hennrich, C. Thomsen, phys. stat. sol. (b) **243**, 3181–3185, (2006)

112. T. Michel, M. Paillet, J. Meyer, V. Popov, L. Henrard, P. Poncharal, A. Zahab, J. Sauvajol, *phys. stat. sol. (b)* **244**, 3986–3991 (2007)
113. P. T. Araujo, A. Jorio, *phys. stat. sol. (b)* **245**, 2201–2204 (2008)
114. J.C. Charlier, P. Lambin, *Phys. Rev. B* **57**, R15037–R15039 (1998)
115. G.G. Samsonidze, R. Saito, N. Kobayashi, A. Gruneis, J. Jiang, A. Jorio, S.G. Chou, G. Dresselhaus, M.S. Dresselhaus, *Appl. Phys. Lett.* **85**, 5703–5705 (2004)
116. L. Yang, J. Han, *Phys. Rev. Lett.* **85**, 154–157 (2000)
117. K.H. Liu, C.H. Jin, X.P. Hong, J. Kim, A. Zettl, E.G. Wang, F. Wang, *Nat. Phys.* **10**, 737–742 (2014)
118. K. Liu, X. Hong, M. Wu, F. Xiao, W. Wang, X. Bai, J.W. Ager, S. Aloni, A. Zettl, E. Wang, *Nat. Commun.* **4**, 1–6 (2013)
119. D.I. Levshov, H.N. Tran, T. Michel, T.T. Cao, V.C. Nguyen, R. Arenal, V.N. Popov, J.L. Sauvajol, A.A. Zahab, M. Paillet, *phys. stat. sol. (b)* **254**, 1700251 (2017)
120. H.N. Tran, J.-C. Blancon, R. Arenal, R. Parret, A.A. Zahab, A. Ayari, F. Vallee, N. Del Fatti, J.-L. Sauvajol, M. Paillet, *Phys. Rev. B* **95**, 205411 (2017)
121. R. Bonnet, A. Lherbier, C. Barraud, M.L. Della Rocca, P. Lafarge, J.-C. Charlier, *Sci. Rep.* **6**, 19701 (2016)
122. S. Zhao, P. Moon, Y. Miyauchi, T. Nishihara, K. Matsuda, M. Koshino, R. Kitaura, *Phys. Rev. Lett.* **124**, 106101 (2020)
123. D.V. Chalin, S.B. Rochal, *Phys. Rev. B* **102**, 115426 (2020)
124. R. Moradian, S. Azadi, H. Refii-Tabar, *J. Phys. Condens. Mat.* **19**, 176209 (2007)
125. D.I. Levshov, R. Parret, H.-N. Tran, T. Michel, T.T. Cao, R. Arenal, V.N. Popov, S.B. Rochal, J.-L. Sauvajol, A.-A. Zahab, *Phys. Rev. B* **96**, 195410 (2017)
126. R. Xiang, T. Inoue, Y. Zheng, A. Kumamoto, Y. Qian, Y. Sato, M. Liu, D. Tang, D. Gokhale, J. Guo, K. Hisama, S. Yotsumoto, T. Ogamoto, H. Arai, Y. Kobayashi, H. Zhang, B. Hou, A. Anissimov, M. Maruyama, Y. Miyata, S. Okada, S. Chiashi, Y. Li, E.I. Kauppinen, Y. Ikuhara, K. Suenaga, S. Maruyama, *Science* **367**, 537–542 (2020)
127. M. Bockrath, D.H. Cobden, J. Lu, A.G. Rinzler, R.E. Smalley, L. Balents, P.L. McEuen, *Nature* **397**, 598–601 (1999)
128. V.V. Deshpande, M. Bockrath, L.I. Glazman, A. Yacoby, *Nature* **464**, 209–216 (2010)
129. H. Ishii, H. Kataura, H. Shiozawa, H. Yoshioka, H. Otsubo, Y. Takayama, T. Miyahara, S. Suzuki, Y. Achiba, M. Nakatake, T. Narimura, M. Higashiguchi, K. Shimada, H. Namatame, M. Taniguchi, *Nature* **426**, 540–544 (2003)
130. Z. Shi, X. Hong, H.A. Bechtel, B. Zeng, M.C. Martin, K. Watanabe, T. Taniguchi, Y.-R. Shen, F. Wang, *Nat. Photonics.* **9**, 515–519 (2015)
131. S. Wang, S. Zhao, Z. Shi, F. Wu, Z. Zhao, L. Jiang, K. Watanabe, T. Taniguchi, A. Zettl, C. Zhou, F. Wang, *Nat. Mater.* **1**, 6 (2020)
132. J. Kong, H.T. Soh, A.M. Cassell, C.F. Quate, H. Dai, *Nature* **395**, 878 (1998)
133. J.A. Misewich, R. Martel, P. Avouris, J.C. Tsang, S. Heinze, J. Tersoff, *Science* **300**, 783 (2003)
134. F. Xia, M. Steiner, Y.-M. Lin, P. Avouris, *Nat. Nanotech.* **3**, 609 (2008)
135. T. Mueller, M. Kinoshita, M. Steiner, V. Perebeinos, A.A. Bol, D.B. Farmer, P. Avouris, *Nat. Nanotech.* **5**, 27 (2010)
136. A. Graf, L. Tropic, Y. Zakharko, J. Zaumseil, M.C. Gather, *Nat. Commun.* **7**, 13078 (2016)
137. R. Watahiki, T. Shimada, P. Zhao, S. Chiashi, S. Iwamoto, Y. Arakawa, S. Maruyama, Y.K. Kato, *Appl. Phys. Lett.* **101**, 141124 (2012)
138. S. Imamura, R. Watahiki, R. Miura, T. Shimada, Y.K. Kato, *Appl. Phys. Lett.* **102**, 161102 (2013)
139. A. Noury, X.L. Roux, L. Vivien, N. Izard, *Nanotechnology* **26**, 345201 (2015)
140. F. Pyatkov, V. Fütterling, S. Khasminkaya, B.S. Flavel, F. Hennrich, M.M. Kappes, R. Krupke, W.H.P. Pernice, *Nat. Photon.* **10**, 420 (2016)
141. S. Moritsubo, T. Murai, T. Shimada, Y. Murakami, S. Chiashi, S. Maruyama, Y.K. Kato, *Phys. Rev. Lett.* **104**, 247402 (2010)

142. I. Sarpkaya, Z. Zhang, W. Walden-Newman, X. Wang, J. Hone, C.W. Wong, S. Strauf, *Nat. Commun.* **4**, 2152 (2013)
143. M. Barkelid, V. Zwiller, *Nat. Photon.* **8**, 47 (2014)
144. M. Eichenfield, R. Camacho, J. Chan, K.J. Vahala, O. Painter, *Nature* **459**, 550 (2009)
145. Y. Gong, B. Ellis, G. Shambat, T. Sarmiento, J.S. Harris, J. Vucković, *Opt. Express* **18**, 8781 (2010)
146. R. Ohta, Y. Ota, M. Nomura, N. Kumagai, S. Ishida, S. Iwamoto, Y. Arakawa, *Appl. Phys. Lett.* **98**, 173104 (2011)
147. J. Riedrich-Möller, L. Kipfstuhl, C. Hepp, E. Neu, C. Pauly, F. Mücklich, A. Baur, M. Wandt, S. Wolff, M. Fischer, S. Gsell, M. Schreck, C. Becher, *Nat. Nanotech.* **7**, 69 (2012)
148. B.J.M. Hausmann, B.J. Shields, Q. Quan, Y. Chu, N.P. de Leon, R. Evans, M.J. Burek, A.S. Zibrov, M. Markham, D.J. Twitchen, H. Park, M.D. Lukin, M. Loncar, *Nano Lett.* **13**, 5791 (2013)